Journal of Materials Chemistry A

RSC Publishing

PAPER

View Article Online
View Journal | View Issue

Cite this: J. Mater. Chem. A, 2013, 1, 13064

Catalytic and synergistic effects on thermal stability and combustion behavior of polypropylene: influence of maleic anhydride grafted polypropylene stabilized cobalt nanoparticles

Qingliang He,[ab] Tingting Yuan,[a] Suying Wei*[b] and Zhanhu Guo*[a]

A novel function of polypropylene grafted with maleic anhydride (PP-*g*-MA) as synergistic additives to effectively reduce the combustion rates of polypropylene (PP) polymer nanocomposites (PNCs) reinforced with *in situ* synthesized cobalt (Co)–cobalt oxide core–shell nanoparticles (NPs) was reported. Two PP-*g*-MAs with molecular weights of ~800 and 2500 g mol^{-1} have been chosen to demonstrate this function. The combustion behaviors and thermal stability of the PP/Co PNCs were evaluated by micro-scale combustion calorimetry (MCC) and thermal gravimetric analysis (TGA). MCC result illustrated that the combustion behaviors of PP were altered by a reduction of ~32% in the peak heat release rate (PHRR) with the incorporation of 20.0 wt% Co NPs; more importantly, further reduction in PHRR more than 50% was observed by adding only 5.0 wt% non-flame retardant PP-*g*-MA into PP/20.0 wt% Co system. This flame retardancy was elucidated through combining MCC with a fast TGA thermal degradation technique. The change of PP thermal degradation pathway by the synergistic and catalytic effects of PP-*g*-MA and Co NPs in the PP matrix was found to be responsible for the decreased combustion rates of PP. Strong interactions between PP and Co NPs formed by the PP-*g*-MA was further confirmed by attenuated total reflection-Fourier transform infrared spectroscopy (ATR-FTIR), which favor the decrease of interfacial tension. Differential scanning calorimetry (DSC) and melt rheometry also demonstrated the surfactant molecular weight dependent melting and crystalline properties, and the melt rheological behaviors of the PP matrix.

Received 11th June 2013
Accepted 16th August 2013

DOI: 10.1039/c3ta12260c

www.rsc.org/MaterialsA

1. Introduction

Magnetic cobalt (Co) nanoparticles (NPs) are of great importance from both an academic and industrial point of view due to their wealth of size dependent structural and catalytic properties.[1] The *in situ* bottom up approach by thermally decomposing neutral organometallic precursors such as dicobalt octacarbonyl ($Co_2(CO)_8$) in organic solvents is one of the most commonly used approaches among the extensively reported chemical approaches for synthesizing Co NPs.[2–6] The advantage of this wet-chemistry method is: through the rapid injecting organometallic precursors into hot solvent, the temporally separated nucleation from particle growth can be realized, which is desirable for producing mono-dispersed colloids.[7] This will facilitate using inert polymers such as polyolefin to serve as the host matrix to these magnetic Co NPs for preparing polymer nanocomposites (PNCs).[6,8] Because the intrinsic steric hindrance from the inert polyolefin hydrocarbon backbone can stabilize the magnetic NPs through counteraction with the strong attractive forces among magnetic NPs derived from their high surface energy, large specific surface area, strong magnetic dipole–dipole interactions and van der Waals forces.[9,10] Therefore, this bottom up method compensated the inert polyolefin for the lack of strong interfacial adhesion with magnetic NPs.

On the other hand, the decrease of interfacial tension through improving the interaction at the polymer–nanofiller interface is also favorable for enhancing the physicochemical property of the resulted PNCs such as thermal stability and flame retardancy.[11,12] Nonetheless, how and what extent the thermal stability and flame retardancy will be improved through reducing the interfacial tension between the polyolefin matrix and fillers like Co NPs is still obscure to date. Meanwhile, since the proposed catalytic effect of the transition metal on the flame retardant PNCs during the 1990s,[13] the catalytic mechanism of Co is still not well documented. Furthermore, the traditionally used small molecular weight surfactants for stabilizing magnetic NPs, such as aliphatic carboxylic acid–oleic acid,[3,4,14,15] organo-amines–dioctylamine,[5] trioctylphosphine (TPO)[16] and TPO oxide (TOPO),[17] have been rarely reported to

[a]Integrated Composites Laboratory (ICL), Dan F. Smith Department of Chemical Engineering, Lamar University, Beaumont, Texas 77710, USA. E-mail: zhanhu.guo@lamar.edu; suying.wei@lamar.edu; Tel: +1 (409) 880 7654; +1 (409) 880 7976

[b]Department of Chemistry and Biochemistry, Lamar University, Beaumont, Texas 77710, USA

integrate into synthesizing magnetic PNCs. The probable reason is that the low thermal stability of small molecular weight surfactant would compromise the physicochemical property of the resulting PNCs. Therefore, a suitable polymeric surfactant for polyolefin-based PNCs reinforced with magnetic NPs is necessary. In addition, the elucidation of its influence on thermal stability and flame retardancy of the thus resulted PNCs is also desirable. For polyolefin-based PNCs with traditional flame retardants such as organo-clay,[11,18] carbon nanotubes (CNT),[19–23] intumescent flame retardant/CNT,[24,25] and layered double hydroxide (LDH) PNCs,[26,27] PP-*g*-MA is a commonly used old-fashion compatibilizer/coupling agent to improve the dispersion of these nanofillers; which can in turn lead to an enhanced flame retardancy and thermal stability. The reason is that the enhancement of interfacial adhesion between the polymer matrix and the nanofillers is often observed due to the reduced interfacial tension. In addition, PP-*g*-MA has been reported to increase the miscibility between immiscible polymer blends through compatibilizing their interfaces.[28,29]

Previously, we have reported the surfactant effect of PP-*g*-MA for preparing magnetic Co and Fe_2O_3 NPs with a manipulated crystalline phase, assembly patterns and magnetic property.[6,30] Strong interfacial interaction has been observed at the interfaces of PP-*g*-MA and those magnetic NPs due to the tight coordination of carboxylic groups (hydrolyzed MA groups) on the surface of the magnetic NPs. In this present work, we demonstrate how this interfacial adhesion between the PP matrix and Co NPs modified by PP-*g*-MA will affect the thermal stability and flame retardancy of the resulting polyolefin-based PNCs reinforced with magnetic Co NPs. The PNCs were synthesized from a one-pot bottom up method, which is ideal to facilitate the PP-*g*-MA to coordinate and stabilize the *in situ* formed Co NPs and to minimize the agglomeration of these magnetic NPs. PP is chosen to be the host polymer matrix due to its miscibility with the PP-*g*-MA attributed to their similarity in the backbone chemical structure. The interfacial interactions between PP-*g*-MA and Co NPs were investigated by Fourier-transform infrared spectroscopy (FT-IR). The morphology of the as-synthesized Co NPs in the PP matrix was illustrated by transmission electron microscopy (TEM). The influence of PP-*g*-MA with two different molecular weights on the thermal stability, flame retardancy, melting and crystalline behaviors as well as melt rheological behaviors of the thus obtained PNCs were systematically studied.

2. Experimental

2.1. Materials

The PP used in this study was supplied by Total Petrochemicals USA, Inc (ρ = 0.9 g cm^{-3}, $M_n \approx$ 40 500). The two PP-*g*-MA (provided by Baker Hughes Inc.) used here were: (1) PP-*g*-MA ($M_n \approx$ 800), designated as PP-*g*-MA (S), is a gel-like propylene-hexene copolymer with one maleic anhydride (MA) group at one terminal and the other MA grafted on the main chain; (2) PP-*g*-MA ($M_n \approx$ 2500), designated as PP-*g*-MA (L), is a solid homopolypropylene with one terminal MA through Alder–ENE reaction.[31] Their chemical structures are shown in Scheme 1.

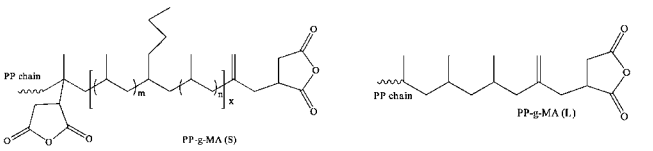

Scheme 1 Chemical structures of PP-*g*-MAs.

Dicobalt octacarbonyl ($Co_2(CO)_8$, stabilized with 1–5% hexane) was obtained from Strem Chemicals, Inc. Solvent xylene (laboratory grade, ρ = 0.87 g cm^{-3}) was purchased from Fisher Scientific. All the chemicals were used as received without any further treatment.

2.2. Polymer nanocomposites preparation

The PP/Co PNCs were synthesized using a typical *in situ* one-pot thermal decomposition method: specifically, 7.5 g PP pellets, 0.5 g PP-*g*-MA (type S, or L) and 100 mL xylene were added into a 500 mL three-neck round bottomed flask. Then, the mixed solution was heated to the refluxing point at approximately 140 °C under mechanical stirring at 200 rpm, and refluxed for 2 h to fully dissolve PP and PP-*g*-MA into a homogeneous transparent solution. After that, the solution was cooled down to around 110 °C; meanwhile, 5.8 g $Co_2(CO)_8$ was dissolved in 120–130 mL xylene in a nitrogen protected glove box. The freshly prepared $Co_2(CO)_8$/xylene solution was injected into the flask to obtain a 20.0 wt% Co loading in PP/PP-*g*-MA system (calculation was based on the pure elemental cobalt weight fraction). While maintaining the stirring speed at 200 rpm and heating temperature at 140 °C, the solution was immediately turned from transparent to brown and then gradually black during an additional 3-h refluxing. The reflux speed was controlled at approximately 1–2 drops per second in order to maintain the smooth reaction. Finally, the solution was cooled down to room temperature in the flask and then poured into a large glass container to evaporate the solvent in the fume hood overnight. The black powders were collected and dried in a vacuum oven at room temperature overnight. The PP/20.0 wt% Co PNCs were also synthesized for comparison (8.0 g PP and 5.8 g $Co_2(CO)_8$ without any PP-*g*-MA). Pure PP was also prepared as reference using the same procedures without adding $Co_2(CO)_8$. The PP-*g*-MA concentration was 5.0 wt% for all the samples except pure PP and PP/20.0 wt% Co PNCs. The experimental Co loading in this study was controlled constantly at 20.0 wt%.

$Co_2(CO)_8$ underwent a series of decomposition reactions, releasing carbon monoxide under constant heating in solution. The thermal decomposition of $Co_2(CO)_8$ was complex and normally went through intermediates such as $Co_4(CO)_{12}$ and $Co_6(CO)_{16}$ (black color), and other unstable mononuclear Co carbonyls ($Co(CO)_x$).[32] After reaction at ~140 °C for several hours, $Co_2(CO)_8$ was fully decomposed and evolved into metallic Co NPs through nuclei generation and particle growth.[32] Meanwhile, a Co oxide layer was formed on the metallic Co particle surface since the Co NPs were further oxidized under open air synthesis conditions.

The 25 mm diameter plate specimens were prepared from the final powders using a hot press molding machine (Model:

Carver 3853-0, USA). First, the powders were added into a cylindrical mold and the mold was placed between two panels in the molding machine. Second, the mold was heated to 180 °C at a heating rate of 20 °C min^{-1} under a pressure of 10 MPa and then maintained at 180 °C for an extra 5–10 min to ensure the formation of compact plates. Finally, the sample was cooled down to room temperature in the mold.

2.3. Characterizations

Fourier transform infrared spectroscopy (Bruker alpha FT-IR spectrometer) with attenuated total reflection (ATR) sampling accessory was utilized to characterize the functional groups of pure PP, PP-*g*-MA, and the PNCs filled with Co NPs over 4000 to 500 cm^{-1}.

The morphology of the Co NPs formed in these resulted PP PNCs was characterized by transmission electron microscopy (TEM) using a FEI TECNAI G2 F20 microscope at a working voltage of 200 kV. The sample was prepared from dropping one droplet of diluted colloidal solution containing the Co NPs on a 400-mesh carbon coated copper grid (Electron Microscopy Sciences). The selected area electron diffraction (SAED) pattern was taken using a large selected-area aperture and recorded by a Gatan SC1000 ORIUS CCD camera. In case the center beam is strong, a needle was placed in the center to block the beam for half of the exposure time (2 s) and then it was immediately removed away from the viewing area, so that the needle appeared in the pattern, which blocked the center strong beam for half of the total exposure time.

Differential scanning calorimetry (DSC) was carried out on a TA Instruments Q2000 calorimeter using typical heat–cool–heat procedures. 5–10 mg sample was sealed in an aluminum pan and heated from room temperature to 180 °C at a heating rate of 10 °C min^{-1} under a N_2 flow rate of approximately 50 mL min^{-1}, then kept constant at 180 °C for 1 min. After that, the specimen was cooled down to room temperature at a cooling rate of 10 °C min^{-1}, followed by a 2nd heating cycle from room temperature to 180 °C at the same heating rate. The data disclosed here were collected from the 1st cooling and the 2nd heating procedures in order to remove the heat history effect on all the specimens.

The thermal stability of the pristine PP and its PNCs was investigated using thermogravimetric analysis (TGA, TA Instruments Q-500). Samples (~10 mg) were heated from room temperature to 700 °C at a constant heating rate of 20 °C min^{-1} under air and N_2 atmospheres, respectively. For simulating the degradation condition of micro-scale combustion calorimetry (MCC), the fast degradation of all the samples was performed at a heating rate of 60 °C min^{-1} (1 °C s^{-1}) in nitrogen. The flow rate was 60 mL min^{-1} under both atmospheres.

Micro-scale combustion calorimetry (MCC) was utilized to evaluate the combustion behaviors/fire hazards by measuring the heat release related parameters through using milligram-sized samples. To be specific, heat release capacity (HRC), heat release rate (HRR) at different temperatures, peak heat release rate (PHRR), temperature at PHRR (T_{PHRR}), and total heat release (THR) can be obtained from MCC. Meanwhile, full width half height (FWHH) and final residue can be calculated. Here, the data was recorded using a "MCC-2" calorimeter manufactured by Govmark Inc. according to the standard method ASTM D7309-2007 (Method A). In a typical measurement, about 5 mg sample was heated from 80 to 650 °C using a heating rate of 1 °C s^{-1} in a continuous stream of nitrogen flowing at 80 mL min^{-1}. The thermal decomposition products (also called as "fuel gases") were mixed with a 20 mL min^{-1} stream of oxygen before entering a 900 °C combustion furnace to complete the non-flaming combustion.

For the PP/Co PNCs without/with PP-*g*-MA, the char residues collected after the MCC test were further studied by X-ray photoelectron spectroscopy (XPS) on a Kratos AXIS 165 system. The scan of each specimen was carried out with a monochromatic Al X-ray source at the anode of 10 kV and a beam current of 15 mA.

The melt rheological behaviors of the PP/PP-*g*-MA matrix and the PNCs were studied using a TA Instruments rheometer (model AR 2000ex). Environmental test chamber (ETC) steel parallel-plate geometry (25 mm in diameter) was used to perform the measurement. A dynamic strain sweep at 1 rad s^{-1} was performed in order to find out the limit of linear viscoelasticity (LVE). Then, the dynamic oscillation frequency was swept from 100 to 0.1 Hz in the LVE range with a strain of 1% at 200 °C under a nitrogen atmosphere. The samples used were circular plate specimens with 25 mm diameter and 2 mm thickness prepared from a hot press.

3. Results and discussion

3.1. FT-IR and TEM

Fig. 1 depicts the FT-IR spectra of PP, two PP-*g*-MA, and their PNCs. The intensive peaks at 1455 and 1375 cm^{-1} were attributed to the absorption of the C–H bending vibration; and the multi-peaks near 3000 cm^{-1} can be indexed to the absorption of the C–H stretching vibration of the hydrocarbon PP backbone.[9] PP-*g*-MA (L) (M_n = 2500) was observed to have all the same absorption peaks as pure PP except one additional peak at 1712 cm^{-1}, which was apparently due to the absorption of the carbonyl (C=O) stretching vibration. PP-*g*-MA (S) was noticed to

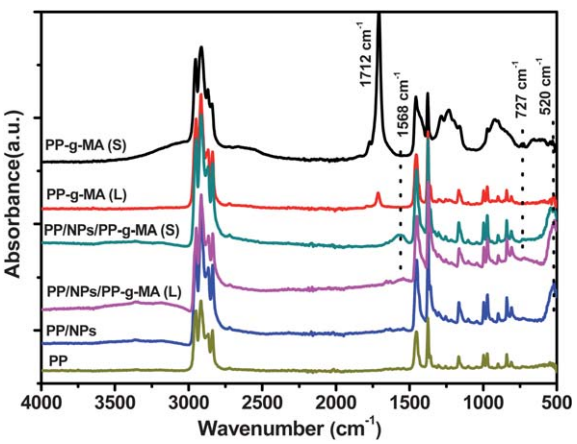

Fig. 1 FT-IR spectra of pure PP, PP-*g*-MA, and their PNCs.

have similar absorption peaks as pure PP along with some different peak shapes around 700–1400 cm^{-1}, which are attributed to its backbone propylene–hexene copolymer characteristics. From 700 to 1400 cm^{-1}, the majority of these peak positions are identical except the peaks are overlapped with a higher intensity for the propylene–hexene samples; which is attributed from the similar backbone of aliphatic C–C and C–H bonds between propylene and hexene. The only one different peak at 727 cm^{-1} is the characteristic of out plane bending vibration of C–H bond. The peak ratio of the 727 and 972 cm^{-1} wavenumber peaks is usually used for determining the hexane contents.[33] Moreover, an intensive C=O stretching vibration peak at 1712 cm^{-1} due to the MA groups was also observed for the PP-*g*-MA (S), indicating a higher MA grafting percentage than that of the PP-*g*-MA (L). For the PP/20.0% Co NPs system, only one new absorption peak at 520 cm^{-1} (Co–O bond, Co in Co^{3+} state) was observed.[34] The PP characteristic peaks were observed to be well maintained, indicating that no chemical bonds were formed between Co NPs and PP backbone when $Co_2(CO)_8$ was thermally decomposed in the PP matrix. TEM image (shown in Fig. 2a) demonstrated a combination of self assembled Co particle chains associated with a large area of agglomerated Co clusters due to the weak stabilization effect of inert PP backbone on these Co NPs. Selected area electron diffraction (SAED) in Fig. 2d further demonstrated the strong ring patterns attributed to the (111), (200), (220) and (222) planes of metallic fcc-Co (PDF# 15-0806), while the other two relatively weak rings are indexed to (102) and (203) planes of Co_2O_3 (PDF# 02-0770). It can thus be concluded that the *in situ* formed Co NPs was covered with an oxide layer. Upon heating, $Co_2(CO)_8$ was decomposed into small metallic Co nuclei and the growth of nuclei led to the formation of nano-scale Co particles. Due to the driving forces from the strong magnetic dipolar forces, high surface tension among Co NPs as well as the weak interaction between the inert PP backbone and Co NPs, some particles were assembled into a short chain structure by the force balance between steric hindrance of PP chain and strong attraction forces among Co NPs.

When adding either one PP-*g*-MA into PP/20.0% Co NPs system, the Co–O absorption peak was noticed to be stable at the same position; however, the intensive characteristic C=O absorption peak at 1712 cm^{-1} was observed to disappear totally, Fig. 1. In addition, a new broad absorption peak at around 1568 cm^{-1} was appeared with 5% PP-*g*-MA (S) in the PP/20.0% Co NPs system. For the PP-*g*-MA (L)/PP/20.0% Co NPs system, the decreased intensity of this new absorption peak (compared with the PP-*g*-MA (S) counterpart) is attributed to the lower MA grafting percentage, which was apparently shown by the much higher intensity of C=O peaks for the PP-*g*-MA (S). It is well known that carboxylic acids can be chemisorbed onto the metal oxide surface, which is evidenced by the shift of characteristic C=O peak at 1700 cm^{-1} to asymmetric and symmetric stretching vibration (CO_2^-) of carboxylate at ~1540 cm^{-1} and 1390–1410 cm^{-1}.[35–37] In our previous work, it was found that PP-*g*-MA can react with trace amounts of moisture in solvent to form carboxylic groups, which can be chemisorbed onto the surface of magnetic NPs during thermal decomposition of organometallic precursor in PP-*g*-MA/xylene solution.[30] Hence, it is concluded that PP-*g*-MA (L/S) was chemisorbed onto the surface of Co NPs during the synthesis of these PP–PP-*g*-MA–Co PNCs. Thus, strong interactions between PP and Co NPs can be transferred by the bridging effect of PP-*g*-MA. When adding 5.0% PP-*g*-MA (L) in the PP/20.0% Co system, the TEM image in Fig. 2b shows that the Co NPs were either separated or assembled into a chain structure with a better dispersion quality compared with the PP/20.0% Co system. In addition, the strong ring patterns in SAED (Fig. 2e) are attributed to the (111), (200), (220), and (311) planes of metallic fcc-Co (PDF# 15-0806). Only

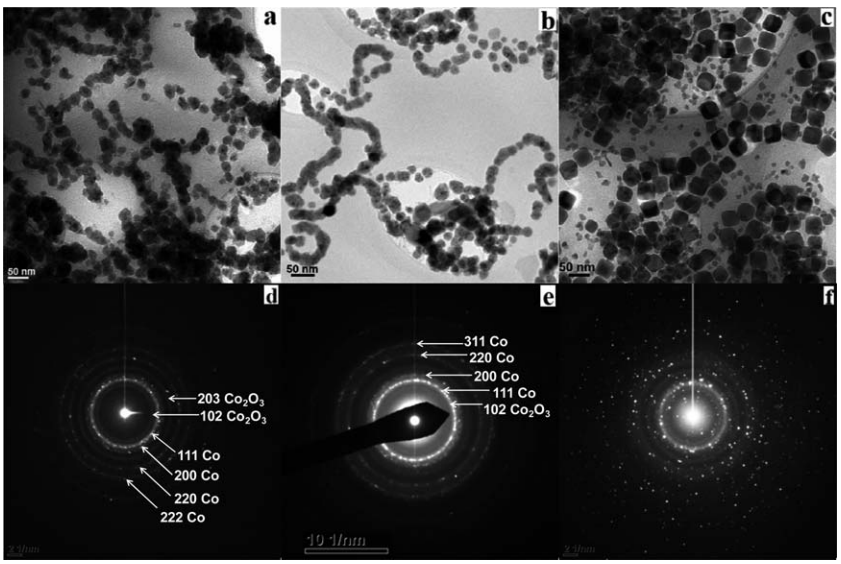

Fig. 2 TEM image of (a) PP/20.0% Co PNCs, and PP/20.0% Co PNCs stabilized with (b) 5.0% PP-*g*-MA (L), (c) 5.0% PP-*g*-MA (S); and (d–f) are the corresponding SAED patterns.

one weak ring pattern overlapped with the (111) plane of fcc-Co can be assigned to Co_2O_3, (102) plane (PDF# 02-0770), indicating less oxidization on the Co surface with addition of PP-*g*-MA (L). Meanwhile, the addition of 5.0% PP-*g*-MA (S) in the PP/20.0% Co nanocomposites is further observed to have the ability to disperse these *in situ* formed Co NPs (polyhedral shapes) separately with clear boundaries (Fig. 2c). From the SAED results shown in Fig. 2f, no noticeable ring patterns can be assigned to the Co oxides, suggesting that the Co NPs stabilized with PP-*g*-MA (S) can prevent oxidization under air. It is clearly demonstrated that PP-*g*-MA can act as a polymeric surfactant to stabilize Co NPs against severe agglomerations.[1,7]

3.2. Melting and crystalline behaviors

Fig. 3a and b show the non-isotherm DSC melting and cooling thermograms of pure PP, PP-*g*-MA, and their PNCs. The quantified results including maximum endothermic melting temperature (T_m), maximum exothermic crystalline temperature (T_c), heat of fusion (ΔH_m), and crystalline fraction (F_c) are summarized in Table 1. The F_c of the studied samples was determined according to eqn (1):

$$F_c = \Delta H_m / [\Delta H_m^o (1 - x)] \quad (1)$$

where, ΔH_m is the measured heat of fusion (integration of the melting peak area under the baseline of DSC curves); ΔH_m^o is the heat of fusion of 100% crystalline PP (here, the theoretical value of ΔH_m^o used is 209 J g^{-1}).[38,39] The x is the loading of the NPs (which is 20.0% constant). For the calculations of these aforementioned parameters, the percentage of PP-*g*-MA (S) in PP and PP/Co system was excluded similar to the particle loading due to the amorphous gel characteristic of PP-*g*-MA (S).

Pure PP has a T_m of 150.7 °C and T_c of 121.5 °C, with ΔH_m of 90.4 J g^{-1} and F_c of 43.3%. It must be noted that, as shown in Fig. 3 (red lines), the absence of both melting and crystalline peaks for pure PP-*g*-MA (S) further confirms its intrinsic amorphous gel-like property. When adding 5% PP-*g*-MA (S) into PP, T_m and T_c were observed to appear at a lower temperature of 145.4 and 105.1 °C, respectively, and ΔH_m was decreased from 90.4 to 76.8 J g^{-1} with a decreased F_c of 38.7%. The probable reason of the decrease in T_m and T_c is that the less ordered crystalline structure such as gel-like amorphous PP-*g*-MA (S) existed in the system.[40] The PP-*g*-MA (L) is a semi-crystalline polymer similar to PP with T_m and T_c observed at 126.4 and 95.8 °C, respectively; meanwhile, ΔH_m was calculated to be 71.3 J g^{-1}. All these parameters were lower than those of pure PP. Nonetheless, when adding 5% PP-*g*-MA (L) into PP, the resulting T_m (150.0 °C) and T_c (118.9 °C) were only slightly affected compared to those of pure PP. However, the ΔH_m was observed to decrease to 84.7 J g^{-1} with a F_c of 40.5%.

Table 1 DSC characteristics of the measured samples

Composition	T_m (°C)	ΔH_m (J g^{-1})	T_c (°C)	ΔH_c (J g^{-1})	F_c (%)
Pure PP	150.7	90.4	121.5	86.6	43.3
PP/20.0% NPs	147.6	67.9	110.6	69.2	40.6
PP-*g*-MA (S)	—	—	—	—	—
PP-*g*-MA (L)	126.4	71.3	95.8	68.3	—
PP/PP-*g*-MA (S)	145.4	76.8	105.1	81.9	38.7
PP/PP-*g*-MA (L)	150.0	84.7	118.9	89.8	40.5
PP/20.0%NPs/PP-*g*-MA (S)	146.4	63.0	110.4	68.2	40.2
PP/20.0%NPs/PP-*g*-MA (L)	145.1	55.8	107.9	60.7	33.4

When adding 20.0 wt% Co NPs in the PP matrix, the corresponding T_m and T_c were decreased to 147.6 and 110.6 °C; and ΔH_m was decreased to 67.9 J g^{-1} with F_c decreased to 40.6%. The decreased T_m is attributed to the crystalline structure in the PP matrix disturbed by the addition of Co NPs.[40] With 20.0 wt% Co particle loading, the formed inter-connected chain nanostructure (TEM image shown in Fig. 2a) can effectively hinder the PP chain mobility and limit the diffusion of PP chains to the growth of polymer crystals. Therefore, the PP chains can only be crystallized at a reduced grain size with more defects, which was consistent with the decreased crystallization peak width, Fig. 3b.[41]

When 5% PP-*g*-MA (L) was added into PP/20.0% Co system, T_m and T_c decreased to 145.1 and 107.9 °C, respectively; meanwhile, ΔH_m decreased from 84.7 to 55.8 J g^{-1} with a decreased F_c of 33.4%. As observed from FT-IR spectra, a strong interfacial adhesion between PP and Co NPs took place by adding PP-*g*-MA in the PP–Co system. Thus, the resulting stronger hindrance of PP chain mobility is considered to be responsible for the decreased PP crystallinity.

The opposite situation was observed when adding 5% PP-*g*-MA (S) in the PP/20% Co NPs system. The corresponding T_m and

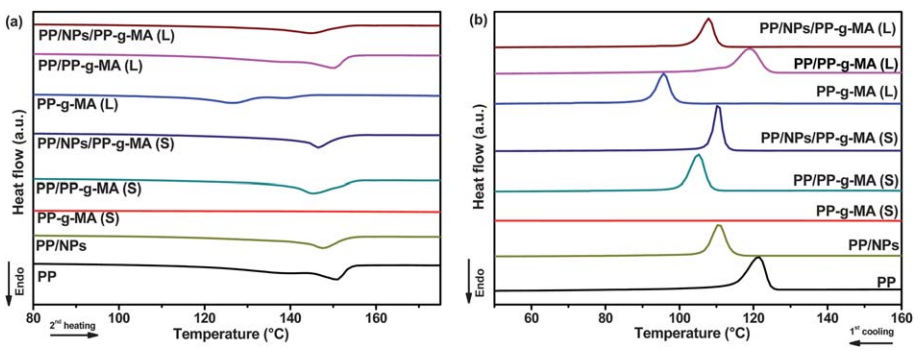

Fig. 3 Heating (a) and cooling (b) of DSC curves for pure PP, PP/PP-*g*-MA and their PNCs.

T_c were increased from 145.4 and 105.1 °C to 146.4 and 110.4 °C, respectively; and F_c increased from 38.7 to 40.2%. The decrease of ΔH_m from 76.8 to 63.0 J g^{-1} is apparently from the addition of 20.0 wt% Co NPs. The increase of T_m and T_c can be explained by the nucleating effect from the Co NPs, which promoted the crystallinity of PP because the well dispersed Co NPs (Fig. 2c) can act as effective nucleating agents and affect the crystallization kinetics of PP.[42–45] From the TEM image in Fig. 2c, it is clear that the separated Co NPs were distributed in the PP matrix in the presence of PP-*g*-MA (S). Since no particle interconnecting network structure formed in the PP matrix and the miscibility of PP-*g*-MA (S) on the surface of Co NPs in the PP matrix, the hindrance of PP chain mobility by these individual Co NPs could be negligible. Therefore, these Co NPs acted as additional nucleating sites for the PP chains so that the T_c and crystallinity of PP were increased correspondingly.

3.3. Thermal stability

Fig. 4a and b depict the TGA curves of PP, PP/PP-*g*-MA, and their PNCs conducted under inert and air atmosphere, respectively. The corresponding data were listed in Tables 2 and 3. Here, the initial degradation temperature (T_{ini}) is defined with a 5% weight loss; and T_{max} (obtained from the differential analysis of TGA curve, DTG) is defined as the temperature when the specimen experiences its peak weight loss rate. The thermal degradation of pure PP was mainly initiated by the thermal scissions of aliphatic C–C backbone associated with hydrogen transfer at the scission sites under nitrogen.[46,47] Specifically, under a heating rate of 20 °C min^{-1}, pure PP has a one stage thermal degradation with T_{ini} of 421.0 °C, and T_{max} of 475.7 °C, and no char residue left at 700 °C.[48] The addition of 5 wt% PP-*g*-MA (L/S) in the PP matrix decreased T_{ini}, however, increased the T_{max}. The decreased T_{ini} is apparently due to the gas volatiles generated from less thermally stable PP-*g*-MA (L/S).[8]

It is noticed that T_{ini} was decreased by 12 °C (from 421.0 to 409.0 °C) and T_{max} was increased with 5.7 °C (from 475.7 to 481.4 °C) after adding 20.0% Co NPs in the PP matrix (Table 2). The combination of 20.0% Co NPs with 5.0% PP-*g*-MA (L/S) in the PP matrix was found to have significantly decreased T_{ini} and slightly increased T_{max}. For the PP-5.0% PP-*g*-MA (S) −20.0% Co NPs system, T_{ini} was decreased to 383.4 °C and T_{max} was increased to 484.6 °C; meanwhile, T_{ini} was decreased to 404.6 °C and T_{max} was increased to 482.2 °C for the PP-5.0% PP-*g*-MA (L) −20.0% Co NPs system. The final residues at 700 °C are 20.2, 22.1 and 20.9% in the PP/Co, PP/Co/PP-*g*-MA (S) and PP/Co/PP-*g*-MA (L) PNCs, respectively. The decreased T_{ini} indicated that earlier weight loss took place when less thermally stable PP-*g*-MA (L/S) was added in the PP/Co system, and the increased T_{max} suggested a better thermal stability at higher temperatures, which is quite similar to the PP/intumescent flame retardant composite but a different mechanism.[25] As confirmed by FT-IR analysis, PP-*g*-MA can be chemisorbed onto the surface of Co NPs; therefore, T_{ini} and T_{max} are assumed to be enhanced upon combining PP matrix with PP-*g*-MA and Co NPs during the inert thermal degradation. However, the decreased T_{ini} suggests a change of degradation pathway, in which more gas volatiles were generated from the initial thermal degradation since the chain scissions took place in the presence of PP-*g*-MA at the early thermal degradation stage of the PP matrix.

Compared with inert thermal degradation, the thermal oxidative stability of the polymer material was prominently reduced by oxidative dehydrogenation accompanied by hydrogen abstraction.[46] The T_{ini} of pure PP was drastically reduced to 266.5 °C in air compared with that of 421.0 °C in nitrogen, and T_{max} was also reduced to 328.0 °C (Table 3). The addition of 5.0 wt% PP-*g*-MA (S) in the PP matrix increased the T_{ini} from 266.5 to 280.4 °C; meanwhile, T_{ini} (266.5 °C) was observed without any change upon adding 5.0 wt% PP-*g*-MA (L) in the PP matrix. In addition, T_{max} was increased with adding either PP-*g*-MA in the PP matrix.

Table 2 TGA characteristics of the measured samples under a nitrogen atmosphere

Composition	T_{ini} (°C) N_2	T_{max} (°C)	Residue at 700 °C (%)
Pure PP	421.0	475.7	0.0
PP/PP-*g*-MA (S)	391.0	481.4	0.0
PP/PP-*g*-MA (L)	415.3	477.3	0.1
PP/20.0% NPs	409.0	481.4	20.2
PP/20.0% NPs/PP-*g*-MA (S)	383.4	484.6	22.1
PP/20.0% NPs/PP-*g*-MA (L)	404.6	482.2	20.9

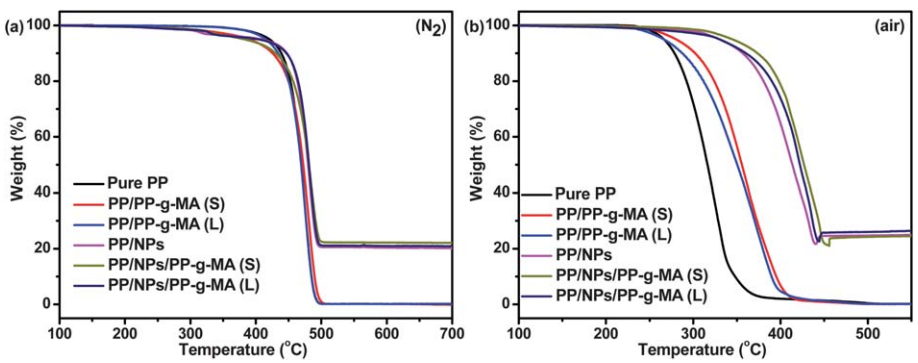

Fig. 4 TGA curves of pure PP and the PNCs under (a) nitrogen and (b) air atmosphere.

Table 3 TGA characteristics of the measured samples under an air atmosphere

Composition	T_{ini} (°C) air	T_{max} (°C)	Residue at 550 °C (%)
Pure PP	266.5	328.0	0.0
PP/PP-*g*-MA (S)	280.4	359.9	0.0
PP/PP-*g*-MA (L)	266.5	375.0	0.0
PP/20.0% NPs	330.6	432.0	25.0
PP/20.0% NPs/PP-*g*-MA (S)	345.0	443.3	24.5
PP/20.0% NPs/PP-*g*-MA (L)	330.4	435.2	26.4

T_{ini} and T_{max} are increased to 330.6 and 432.0 °C when 20.0% Co NPs were added into PP matrix, which were 64.1 and 104.0 °C higher than those of pure PP. The oxidative residue of the PP/Co PNCs at 550 °C was 25.0%, indicating that the oxidation of these Co NPs took place under 550 °C in air. It is concluded that the Co NPs significantly enhanced the thermal oxidative stability of the PP matrix through deferring oxidative degradation. More importantly, T_{ini} and T_{max} were further increased to 345.0 and 443.3 °C (14.4 and 11.3 °C higher than PP/Co, or 78.5 and 115.3 °C higher than pure PP) when 5.0% PP-*g*-MA (S) was added in the PP-20.0% Co NPs system. However, the PP-*g*-MA (L) was found to have a limited effect in further increasing the T_{ini} and T_{max} of the PP matrix when added into PP-20.0 wt% Co system. The difference in the MA percentage between PP-*g*-MA (L) and PP-*g*-MA (S) was believed to be responsible for the difference in the thermal oxidative stability of the PP/PP-*g*-MA/Co system. The enhanced thermal oxidative stability by PP-*g*-MA (S) is obviously attributed to the enhanced interfacial adhesion effect between PP and Co NPs, which requires more energy to decompose the PP/PP-*g*-MA/Co complex in air; meanwhile, this effect is limited by less bonding through PP-*g*-MA (L) on Co NPs.[8]

3.4. Combustion behaviors

MCC was utilized to further assess the fire hazards of pure PP, PP/20.0 wt% Co PNCs, and PP/20.0% Co PNCs stabilized with two different molecular weight PP-*g*-MA. Fig. 5 depicts the HRR *vs.* temperature curves and Table 4 shows the corresponding heat release parameters. HRR is the single most important parameter to assess the fire hazard of one flammable material.[49] The higher PHRR material behaves under a specific heat flux, the more dangerous it will act under a fire accident. Pure PP is a highly flammable material as the PHRR observed here of 1513.0 W g^{-1}. Adding 5% PP-*g*-MA (L/S) only slightly decreased the flammability as indicated by the small amounts of reduction in HRC, PHRR, and THR (Table 4); which were apparently due to less gas fuel generated from the oxygen-containing PP-*g*-MA (L/S) than pure hydrocarbon PP. Meanwhile, the initial thermal decomposition and T_{PHRR} were barely changed.

In the case of the PP-20.0 wt% Co NPs PNCs, PHRR was decreased from 1513.0 to 1024.0 W g^{-1} (~32.3% reduction), THR was decreased from 40.6 to 27.7 kJ g^{-1} (~31.8% reduction); and the initial decomposition temperature was enhanced upon adding the Co NPs (Fig. 5), which is consistent with the increased thermal stability observed from TGA under N_2. Apparently, with excluding the dilution of combustible PP

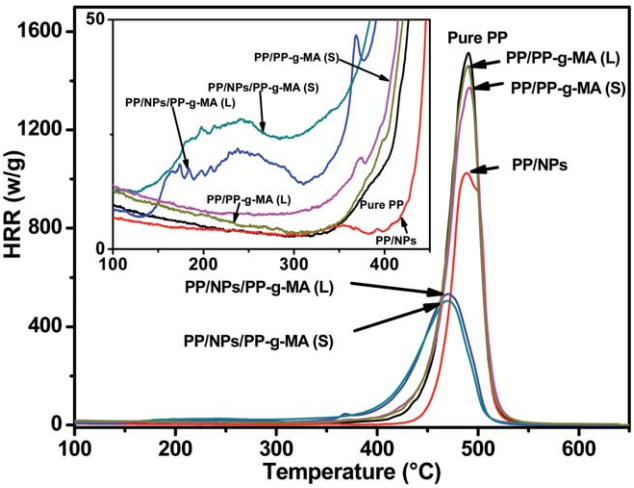

Fig. 5 Heat release rate curves of pure PP, PP/PP-*g*-MA, PP/20.0% Co PNCs, and PP/20.0% Co PNCs stabilized with two different molecular weight PP-*g*-MAs. Inset is enlarged initial low temperature decomposition between 100 and 400 °C.

through the 20.0 wt% non-combustible Co loading, an additional 12.3% decrease in HRR and 11.8% decrease in THR indicated a flame retardancy effect of these *in situ* synthesized Co NPs. A barrier effect from these Co NPs was believed to be responsible for the flame retardancy. During the decomposition, heat and mass transfers between gas- and condense-phases were slowed down by forming an insulating layer when these PNCs were exposed under heat, and thus fast decomposition of the polymeric PP matrix was suppressed.[50] Therefore, the HRR reduction suggests a slower speed of combustible volatiles generated from the random chain scission of PP backbones in the presence of Co NPs.

Synergistic effect in reducing flammability was observed when adding 5.0% both PP-*g*-MA in the PP-20.0 wt% Co NPs system (Fig. 5). HRC and PHRR were observed to decrease sharply, *i.e.*, PHRR was further decreased ~50% (from 1024.0 to 532.4 W g^{-1} in the case of PP–PP-*g*-MA (L)–Co PNCs, or to 500.8 W g^{-1} in the case of PP–PP-*g*-MA (S)–Co PNCs) when 5.0% non-flame retardant PP-*g*-MA was added in the PP–Co PNCs. Meanwhile, THR was further slightly decreased from 27.7 to 25.6 kJ g^{-1} with the addition of 5.0% PP-*g*-MA (L); or to 25.1 kJ g^{-1} with the addition of 5.0% PP-*g*-MA (S) into PP-20.0% Co PNCs. This remarkable decrease in the flammability of PP by a non-flame retardant additive – PP-*g*-MA has never been reported. Although the conventional synergistic effect (such as nitrogen–phosphorus,[48,51,52] phosphorus–silicon,[53,54]) on flame retardant PNCs has been extensively studied and reported, the synergistic effect between PP–MA and Co NPs have rarely been demonstrated. In addition, when either PP-*g*-MA was added in the PP-20.0% Co system, a small amount of HRR was observed during the initial thermal decomposition stage (around 100–300 °C) and T_{PHRR} was decreased to 471.0 °C (shown in the inset of Fig. 5).

3.5. XPS analysis and flame retardancy mechanism

XPS analysis was further carried out to identify the atomic composition of solid char residues of the PP/Co PNCs after the

Table 4 Heat release parameters of the measured samples

Composition	HRC (J g^{-1} k^{-1})	PHRR (W g^{-1})	PHRR reduction (%)	T_{PHRR} (°C)	THR (kJ g^{-1})	FWHH (s)
Pure PP	1187.0	1513.0	—	490.4	40.6	24.2
PP/PP-*g*-MA (L)	1150.0	1454.0	3.9	491.1	40.3	25.1
PP/PP-*g*-MA (S)	1077.0	1366.0	9.7	489.9	39.8	25.9
PP/20.0% NPs	809.0	1024.0	32.3	489.9	27.7	23.7
PP/20.0% NPs/PP-*g*-MA (L)	417.0	532.4	64.8	471.0	25.6	39.7
PP/20.0% NPs/PP-*g*-MA (S)	395.0	500.8	66.9	471.0	25.1	41.0

MCC test and to determine their local chemical environment (here we focused on investigating the valence state of the Co NPs after combustion). The XPS spectra and the detailed data of the C1s, O1s, and Co2p spectra are shown in Fig. 6a–c and Table 5. For the C1s spectrum (Fig. 6a), the peak at around 284.6 eV is attributed to C–C in the aliphatic species. When combining either PP-*g*-MA (L) or PP-*g*-MA (S) with Co NPs in the PP matrix, the peak position was barely changed, indicating the same carbon species left after the combustion of these PP/Co PNCs. For O1S spectrum (Fig. 6b), compared with PP/Co PNCs, the O1s peak shifted from higher (531.5 eV) to lower binding energy after addition of 5.0 wt% PP-*g*-MA (L) or PP-*g*-MA (S) in the PP/Co system (Table 5). Usually, the O 1s peak of PP-*g*-MA can be deconvoluted into two component peaks: the peak at 532.7 eV arises from the carbonyl oxygen (C═O) of the maleic anhydride, whereas the peak at 533.8 eV arises from the ether oxygen (C–O–C).[55] Thus, the lower binding energy indicates that the oxygen environments are changed by the Co. For Co 2p spectrum (Fig. 6c), the Co $2p_{3/2}$ and Co $2p_{1/2}$ peaks are located at ~778.5 and 793.8 eV, respectively, which are consistent with the reported metallic Co NPs.[56] Meanwhile, the shoulder peaks at ~780 and 782 eV can be assigned to Co^{3+} $2p_{3/2}$ and Co^{2+} $2p_{3/2}$, respectively; which are in good agreement with the reported Co_3O_4.[57] This indicates that the Co oxides are converted to Co_3O_4 after the combustion in MCC. From Table 5, it is clear that the carbon species mass percentage increased sharply from 61.08% for the PP/20.0 wt% Co PNCs to 78.08% for PP–PP-*g*-MA (L)–20.0 wt% Co PNCs, and to 80.92% for PP–PP-*g*-MA (S)–20.0 wt% Co PNCs; corresponding to 83.16%, 89.43%, and 90.89% atomic percentage of carbon, respectively. This further indicates that the combination of Co NPs and PP-*g*-MA in the PP matrix can facilitate the char formation at high temperature combustion through their synergistic and catalytic effect, which can effectively decrease the heat release rates of PP.

In order to elucidate the synergism between PP-*g*-MA and Co NPs in dramatically reducing the flammability of PP matrix, a fast thermal degradation test was performed by TGA using the same condition as MCC measurements – a heating rate of 60 °C

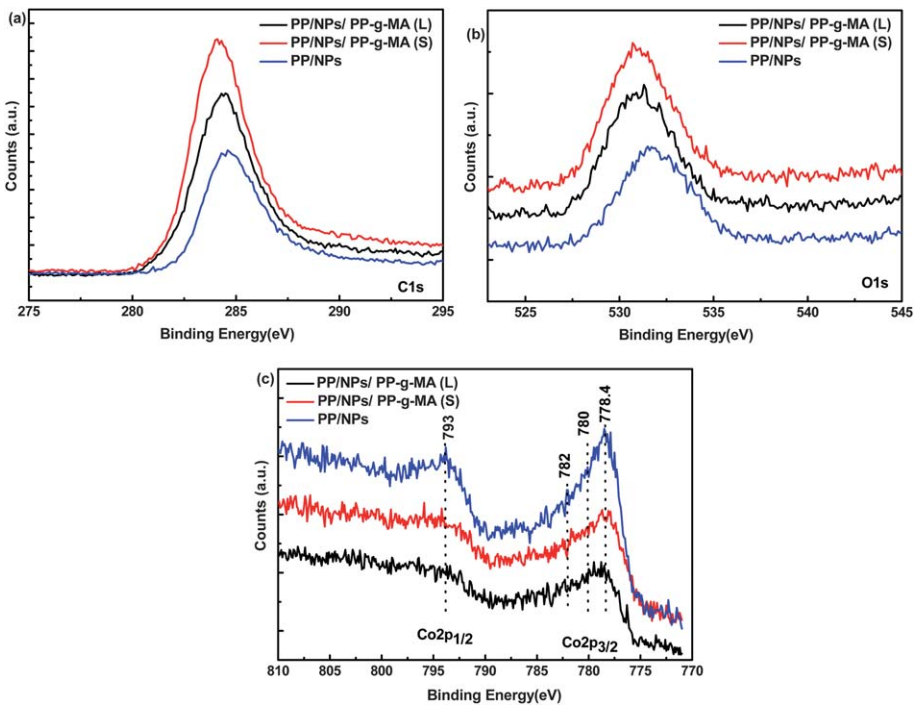

Fig. 6 (a) C1s, (b) O 1s, and (c) Co 2p XPS spectra of the char residues collected from the MCC test of PP/Co PNCs with/without PP-*g*-MA.

Table 5 Detailed XPS data of the char residues for the PP/Co PNCs

Sample	Peak BE (eV)	Position BE (eV)	Atomic conc. (%)	Mass conc. (%)
PP/NPs	C 1s	284.60	83.16	61.08
	O 1s	531.50	8.29	8.11
	Co 2p	778.50	8.55	30.81
PP/NPs/PP-*g*-MA (L)	C 1s	284.30	89.43	78.08
	O 1s	531.30	7.49	8.71
	Co 2p	778.80	3.08	13.21
PP/NPs/PP-*g*-MA (S)	C 1s	284.10	90.89	80.92
	O 1s	530.70	6.51	7.72
	Co 2p	778.10	2.60	11.37

min^{-1} (1 °C s^{-1}) under nitrogen (TGA and DTG curves shown in Fig. 7). MCC measurements here were performed using an inert sample thermal degradation procedure to pyrolyze the sample into combustible gas volatiles followed by a non-flaming oxidation of these volatiles. The fast thermal degradation by TGA can illustrate the dynamic sample weight loss under temperature ramping at a constant high heating rate (1 °C s^{-1}); meanwhile, the derivative weight loss (%/°C) from the inset of Fig. 7 can reproduce the thermal degradation stage of MCC clearly. Therefore, the degradation and weight loss processes can be demonstrated simultaneously.

It is noticed from Fig. 5 that the addition of 5.0% PP-*g*-MA (L/S) barely decreased the initial thermal degradation temperature of PP; while 20.0% Co NPs increased the initial thermal degradation of PP as evidenced by the higher thermal degradation temperature compared with that of pure PP (no detectable HRR increase before 400 °C, shown in the inset of Fig. 5). However, the degradation of PP-5.0% PP-*g*-MA (L/S)–20.0% Co NPs was definitely altered by the evidence of: broad HRR peaks appearing in the range of 130–310 °C (insert of Fig. 5), and ~18.0% weight loss within the thermal degradation temperature of 100–310 °C from the TGA curves (Fig. 7). When exposed to heat flux at elevated temperature from 80 to 650 °C, the inert thermal degradation of PP was initiated primarily by chain scission and chain transfer; then reductions in molecular weight were first observed at 227 to 247 °C and gas volatiles became significant above 302 °C. Finally, ignition of PP was observed at a surface temperature of 337 °C,[58] which is consistent with the initial HRR jump at ~330 °C observed from MCC. Meanwhile, the addition of 5.0% PP-*g*-MA (L/S) has a limited influence on initiating the degradation of the PP matrix. With adding 20.0% Co NPs, only shielding effects were responsible for reducing the HRR through slowing and delaying the release of gas volatiles.[50] When adding PP-*g*-MA together with Co NPs in the PP matrix, the catalytic effect was responsible for lowering the initial thermal degradation temperature of the resulted PNCs (from 330 °C for pure PP to ~100–130 °C for the PNCs), and led to a smaller HRR in the range of 100–310 °C due to a small amount of gas volatiles released from the bulk material. A probable mechanism includes random chain scission of the C–C bond of the PP backbone to generate hydrocarbon radicals during initial decomposition, the formation of lower hydrocarbons such as propylene from further degradation of these hydrocarbon radicals, the β-scission and abstraction of H radicals from other hydrocarbons to produce a new hydrocarbon radicals during the propagation stage, and finally the disproportionate or re-combination of two radicals as a termination reaction.[59] Meanwhile, slightly similar to the "smoldering" fire, a substantial fraction of the total mass of PP/5.0% PP-*g*-MA (L/S)/Co PNCs (~18.0%) was consumed during 100–310 °C subjected to a slow heat release process, effectively decreased the total available gas fuels, which would generate a large quantity of heat under higher temperatures. In addition, the strong interfacial adhesion between Co NPs and PP matrix through PP-*g*-MA was responsible for the sharply suppressed mass loss rate as observed reduction in PHRR (Fig. 5 and 7). One can also observe that FWHH of the PP/PP-*g*-MA/Co PNCs was much wider than those of pure PP, PP/PP-*g*-MA and PP/Co PNCs (Table 4), further indicating a longer combustion period upon introducing the PP-*g*-MA and Co NPs in the PP matrix. This is another sign of reduced fire hazard of the PP/PP-*g*-MA/Co PNCs. Although the catalytic effect has been long proposed to be responsible for enhancing the flame retardancy for the PNCs incorporated with flame retardants with transitional metals, this synergistic catalytic effect from combining Co NPs with non-flame retardant PP-*g*-MA is reported for the first time.

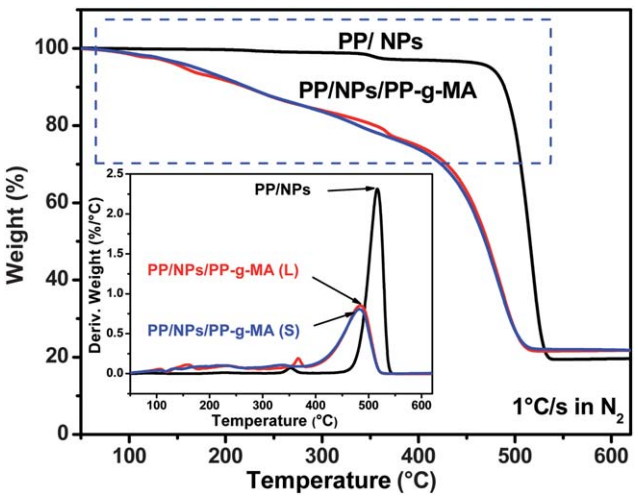

Fig. 7 TGA and DTG curves of PP/20.0% Co MPNCs and PP/20.0% Co PNCs stabilized with two PP-*g*-MAs under a heating rate of 1 °C s^{-1} (60 °C min^{-1}).

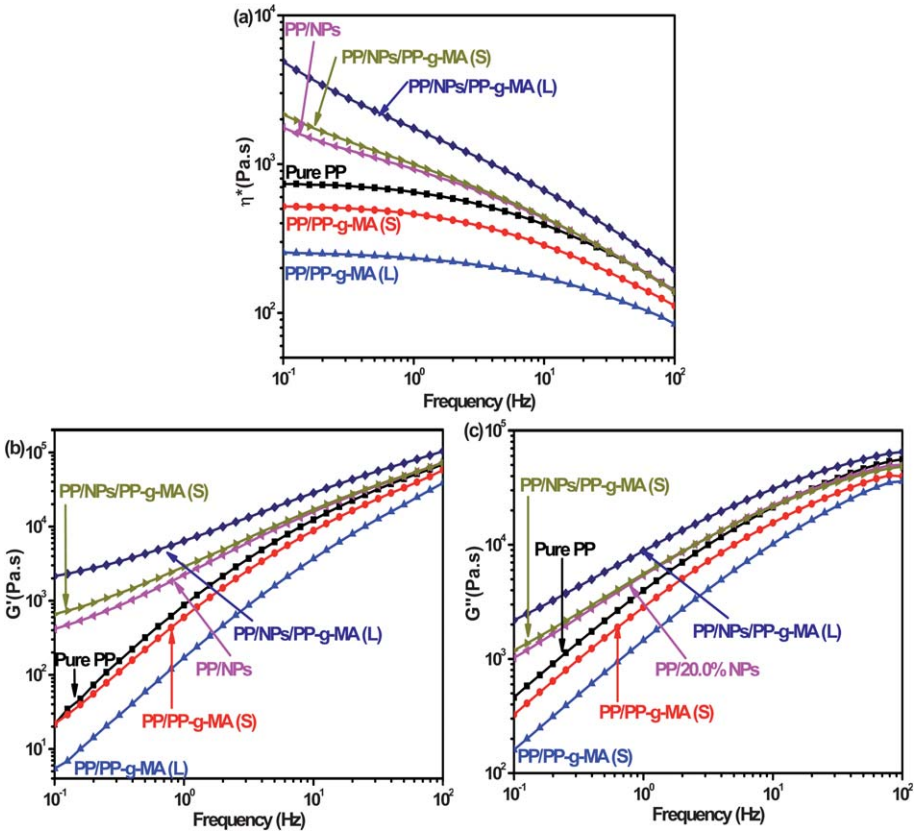

Fig. 8 Melt rheological properties (a) complex viscosity, (b) storage modulus, and (c) loss modulus of PP and its PNCs.

3.6. Viscoelastic behaviors

In general, differences in melting rheological behaviors have provided insights into the internal structure of polymers or PNCs. Information including percolated network structure, particle dispersion, and the interfacial interaction between polymer matrix and the nanofillers can be obtained.[60] Fig. 8 illustrated the frequency sweep curves for complex viscosity (η^*, Fig. 8a), storage modulus (G', Fig. 8b) and loss modulus (G'', Fig. 8c) of pure PP, PP/PP-*g*-MA blends, and their PNCs at 200 °C from 0.1 to 100 Hz.

The PP/5 wt% 5.0% PP-*g*-MA (L/S) blends showed a similar trend in viscosity as pure PP: Newtonian-type flow behavior in the low oscillation frequency region as indicated by a frequency independent fluid viscosity type followed by a shear thinning (η^* decreases with an increase of oscillation frequency) behavior[61,62] up to 100 Hz. However, within the whole oscillation frequency range, the η^* values of PP/5 wt% 5.0% PP-*g*-MA (L/S) blends were found to be lower than that of pure PP. G' and G'' also showed the same trend. Apparently, the plasticization effect of PP-*g*-MA due to its lower molecular weight (M_n of 800, 2500 compared with 40 500 of PP) can lead to the decrease in viscosity.[24,63,64]

Generally, polymeric materials with higher molecular weight demonstrate more viscous than their lower molecular weight counterparts. In addition, less viscous fluid of the relatively short PP-*g*-MA than long chain PP was also reported.[65] Hence, PP/PP-*g*-MA blends exhibited a lower viscosity, G' and G'' than pure PP.[66,67] The higher viscosity of PP/PP-*g*-MA ($M_n = 800$) than that of PP/PP-*g*-MA ($M_n = 2500$) might be due to the fact of amorphous gel-like characteristics of PP-*g*-MA (S), which is detrimental to the plasticity effect. Another probable reason is that more free volume created by the longer PP-*g*-MA chains than the shorter counterpart can further decrease the viscosity.

With the addition of 20.0 wt% Co NPs in the PP matrix, the viscosity η^* demonstrated a typical shear thinning behavior; moreover, η^* was found to increase further within the entire oscillation frequency range when 5.0 wt% PP-*g*-MA (L/S) was introduced in the PP/20 wt% Co PNCs. An unexpected observation was found that the addition of 5.0% PP-*g*-MA (L) leads to a much higher viscosity compared to that of 5.0% PP-*g*-MA (S). At high particle loading like 20.0 wt%, the PNCs usually showed filler dominated fluid dynamics rather than polymer melt as indicated by the monotonically decreased viscosity within the whole oscillation frequency for all the PP/Co and PP/PP-*g*-MA/Co PNCs. In addition, the wide separation in the low frequency range while the slight separation within the high frequency range of G' and G'' suggests the increased solid-like properties of the polymeric matrix when the oscillation frequency is low enough for these NPs restrict the mobility of the polymer chain.[68] Upon heating to melt state, PP chains experienced a total relaxation; however, the chain relaxation and relative motion were strongly restrained after incorporation with high loading NPs, *i.e.* 20.0 wt% Co NPs. Thus, all the PP PNCs became "stiffer" as indicated by the simultaneously increased

viscosity. As observed from TEM, it is noticed that the interconnected network structure was formed in the PP/20.0 wt% Co PNCs, which can also prove this filler dominated fluid dynamics. Meanwhile, a less entangled inter-network particle structure was also observed in the PP matrix when 5.0 wt% PP-*g*-MA (L) was incorporated into PP/20.0 wt% Co PNCs. However, the unexpected increase in viscosity was observed; which can only be explained by the stronger interfacial interactions between filler and PP matrix improved by the coupling/bridge effect of PP-*g*-MA. These effects in turn led to a lower mobility of the polymer chain, making the PP PNCs more rigid and solid-like. In PP/5.0% PP-*g*-MA (S)/20.0 wt% Co PNCs, TEM observations demonstrated the polyhedral shaped Co NPs were well dispersed in the PP matrix without any percolation. This lack of percolated particle network leads to a decreased viscosity compared to that of PP/5.0% PP-*g*-MA (L)/20.0 wt% Co PNCs due to the obviously weaker restriction of the polymer chain movement. Meanwhile, the viscosity was found to be still higher than that of the PP/20.0 wt% Co PNCs; which is again the evidence of strong interfacial interaction between Co NPs and PP matrix through the coupling effect of PP-*g*-MA. Hence, the adhesion between the filler and polymeric matrix can be significantly enhanced since the Co particle surface "wrapped" with PP-*g*-MA short chain can favor the entanglements among the PP matrix. This can also be evidenced by the higher G' and G'' for the PP/PP-*g*-MA/Co PNCs than PP/Co PNCs since the more obvious plateau formed at the low frequency area can only be attributed to the enhanced interfacial interactions between the fillers and polymer matrix.[69]

4. Conclusion

The catalytic and synergistic effect on significantly reducing the flammability of PP has been demonstrated by adding a small amount (5.0 wt%) of non-flame retardant additive – PP-*g*-MA – in the PP PNCs reinforced with the *in situ* synthesized Co NPs. The stabilization of Co NPs by PP-*g*-MA leads to a strong interfacial adhesion between the Co NPs and PP matrix through the coupling effect of PP-*g*-MA; which reflects the increase of thermal and thermal oxidative stability of the resulting PP PNCs. In addition, catalytic and synergistic effects through combining Co NPs with PP-*g*-MA have further changed the thermal degradation pathway of PP by accelerating the low temperature weight loss rate (observed from MCC) and facilitating the high temperature char formation (confirmed from XPS). Those changes further result in ~50.0% reduction in PHRR compared with PP/Co PNCs without PP-*g*-MA. This high efficiency in suppressing the combustion rates through combining the non-flame retardant additive of PP-*g*-MA with the Co NPs will give rise to further insight to the design of novel catalytic flame retardant composition. Meanwhile, the observed morphology dependent melt rheological behaviors with the changes in viscosity, storage and loss modulus can also give insight to the difference in assembly patterns of the *in situ* formed NPs in the PP matrix and the interfacial adhesion between the polymer matrix and the nanofillers.

Acknowledgements

This project is supported by the Seeded Research Enhancement Grant from Lamar University. Partial financial support from National Science Foundation - Chemical and Biological Separations (CBET: 11-37441) managed by Dr Rosemarie D. Wesson is appreciated. We also appreciate the support from National Science Foundation Nanoscale Interdisciplinary Research Team and Materials Processing and Manufacturing (CMMI 10-30755) to purchase TGA and DSC. Partial financial support from Baker Hughes Inc. is also appreciated. S.W. thanks the Welch Foundation (V-0004).

References

1 V. F. Puntes, K. M. Krishnan and A. P. Alivisatos, *Science*, 2001, **291**, 2115–2117.
2 V. Baranauskas, III, M. Zalich, M. Saunders, T. G. S. Pierre and J. Riffle, *Chem. Mater.*, 2005, **17**, 5246–5254.
3 A. Lagunas, C. Jimeno, D. Font, L. Solà and M. A. Pericàs, *Langmuir*, 2006, **22**, 3823–3829.
4 G. Cheng, C. L. Dennis, R. D. Shull and A. R. H. Walker, *Langmuir*, 2007, **23**, 11740–11746.
5 Y. Bao, W. An, C. H. Turner and K. M. Krishnan, *Langmuir*, 2010, **26**, 478–483.
6 Q. He, T. Yuan, Z. Luo, N. Haldolaarachchige, D. P. Young, S. Wei and Z. Guo, *Chem. Commun.*, 2013, **49**, 2679–2681.
7 S. Sun and C. Murray, *J. Appl. Phys.*, 1999, **85**, 4325–4330.
8 Q. He, T. Yuan, X. Zhang, Z. Luo, N. Haldolaarachchige, L. Sun, D. P. Young, S. Wei and Z. Guo, *Macromolecules*, 2013, **46**, 2357–2368.
9 J. Zhu, S. Wei, Y. Li, L. Sun, N. Haldolaarachchige, D. P. Young, C. Southworth, A. Khasanov, Z. Luo and Z. Guo, *Macromolecules*, 2011, **44**, 4382–4391.
10 Q. He, T. Yuan, J. Zhu, Z. Luo, N. Haldolaarachchige, L. Sun, A. Khasanov, Y. Li, D. P. Young and S. Wei, *Polymer*, 2012, **53**, 3642–3652.
11 Y. Tang, Y. Hu, B. Li, L. Liu, Z. Wang, Z. Chen and W. Fan, *J. Polym. Sci., Part A: Polym. Chem.*, 2004, **42**, 6163–6173.
12 S. Zhang and A. R. Horrocks, *Prog. Polym. Sci.*, 2003, **28**, 1517–1538.
13 M. Lewin, *J. Fire Sci.*, 1999, **17**, 3–19.
14 G. Cheng, D. Romero, G. T. Fraser and A. R. H. Walker, *Langmuir*, 2005, **21**, 12055–12059.
15 I. Robinson, M. Volk, L. D. Tung, G. Caruntu, N. Kay and N. T. K. Thanh, *J. Phys. Chem. C*, 2009, **113**, 9497–9501.
16 G. Liu, X. Yan, Z. Lu, S. A. Curda and J. Lal, *Chem. Mater.*, 2005, **17**, 4985–4991.
17 Z. Zhou, G. Liu and D. Han, *ACS Nano*, 2009, **3**, 165–172.
18 C. Chen and D. G. Baird, *Polymer*, 2012, **53**, 4178–4186.
19 Y. Wang, J. Wu and F. Wei, *Carbon*, 2003, **41**, 2939–2948.
20 T. Kashiwagi, E. Grulke, J. Hilding, K. Groth, R. Harris, K. Butler, J. Shields, S. Kharchenko and J. Douglas, *Polymer*, 2004, **45**, 4227–4239.
21 J. F. Berret, N. Schonbeck, F. Gazeau, D. El Kharrat, O. Sandre, A. Vacher and M. Airiau, *J. Am. Chem. Soc.*, 2006, **128**, 1755–1761.

22 S. H. Lee, E. Cho, S. H. Jeon and J. R. Youn, *Carbon*, 2007, **45**, 2810–2822.
23 T. Kashiwagi, M. Mu, K. Winey, B. Cipriano, S. Raghavan, S. Pack, M. Rafailovich, Y. Yang, E. Grulke and J. Shields, *Polymer*, 2008, **49**, 4358–4368.
24 P. Song, L. Xu, Z. Guo, Y. Zhang and Z. Fang, *J. Mater. Chem.*, 2008, **18**, 5083–5091.
25 P. Song, Y. Shen, B. Du, M. Peng, L. Shen and Z. Fang, *ACS Appl. Mater. Interfaces*, 2009, **1**, 452–459.
26 S. P. Lonkar, S. Morlat-Therias, N. Caperaa, F. Leroux, J. L. Gardette and R. P. Singh, *Polymer*, 2009, **50**, 1505–1515.
27 D.-Y. Wang, A. Das, F. R. Costa, A. Leuteritz, Y.-Z. Wang, U. Wagenknecht and G. Heinrich, *Langmuir*, 2010, **26**, 14162–14169.
28 W. Chow, Z. Mohd Ishak, J. Karger-Kocsis, A. Apostolov and U. Ishiaku, *Polymer*, 2003, **44**, 7427–7440.
29 Y. Tang, Y. Hu, L. Song, R. Zong, Z. Gui and W. Fan, *Polym. Degrad. Stab.*, 2006, **91**, 234–241.
30 Q. He, T. Yuan, S. Wei, N. Haldolaarachchige, Z. Luo, D. P. Young, A. Khasanov and Z. Guo, *Angew. Chem., Int. Ed.*, 2012, **51**, 8842–8845.
31 Y. Yang, M. C. Gupta, K. L. Dudley and R. W. Lawrence, *Nano Lett.*, 2005, **5**, 2131–2134.
32 V. F. Puntes, D. Zanchet, C. K. Erdonmez and A. P. Alivisatos, *J. Am. Chem. Soc.*, 2002, **124**, 12874–12880.
33 D. A. Godfrey, *US Pat.*, 4,929,509, 1990.
34 F. Mohandes, F. Davar and M. Salavati-Niasari, *J. Magn. Magn. Mater.*, 2010, **322**, 872–877.
35 G. B. Deacon and R. J. Phillips, *Coord. Chem. Rev.*, 1980, **33**, 227–250.
36 M. K. Nazeeruddin, R. Humphry-Baker, P. Liska and M. Grätzel, *J. Phys. Chem. B*, 2003, **107**, 8981–8987.
37 J. Rochford, D. Chu, A. Hagfeldt and E. Galoppini, *J. Am. Chem. Soc.*, 2007, **129**, 4655–4665.
38 E. D. Carlson, M. T. Krejchi, C. D. Shah, T. Terakawa, R. M. Waymouth and G. G. Fuller, *Macromolecules*, 1998, **31**, 5343–5351.
39 A. Rozanski, A. Galeski and M. Debowska, *Macromolecules*, 2011, **44**, 20–28.
40 X. Xia, S. Cai and C. Xie, *Mater. Chem. Phys.*, 2006, **95**, 122–129.
41 Y. Li and X. S. Sun, *Biomacromolecules*, 2010, **11**, 1847–1855.
42 C. Saujanya and S. Radhakrishnan, *Polymer*, 2001, **42**, 6723–6731.
43 R. Masirek, E. Szkudlarek, E. Piorkowska, M. Slouf, J. Kratochvil and J. Baldrian, *J. Polym. Sci., Part B: Polym. Phys.*, 2010, **48**, 469–478.
44 J. Z. Xu, C. Chen, Y. Wang, H. Tang, Z. M. Li and B. S. Hsiao, *Macromolecules*, 2011, **44**, 2808–2818.
45 S. W. Kuo and F. C. Chang, *Prog. Polym. Sci.*, 2011, **36**, 1649–1696.
46 T. Kashiwagi, E. Grulke, J. Hilding, R. Harris, W. Awad and J. Douglas, *Macromol. Rapid Commun.*, 2002, **23**, 761–765.
47 C. A. Wilkie and A. B. Morgan, *Fire retardancy of polymeric materials*, CRC, 2009.
48 Q. He, H. Lu, L. Song, Y. Hu and L. Chen, *J. Fire Sci.*, 2009, **27**, 303–321.
49 V. Babrauskas and R. D. Peacock, *Fire Saf. J.*, 1992, **18**, 255–272.
50 X. Wang, L. Song, H. Yang, W. Xing, H. Lu and Y. Hu, *J. Mater. Chem.*, 2012, **22**, 3426–3431.
51 H. Yang, C. Q. Yang and Q. He, *Polym. Degrad. Stab.*, 2009, **94**, 1023–1031.
52 S. Nie, Y. Hu, L. Song, Q. He, D. Yang and H. Chen, *Polym. Adv. Technol.*, 2008, **19**, 1077–1083.
53 Q. He, L. Song, Y. Hu and S. Zhou, *J. Mater. Sci.*, 2009, **44**, 1308–1316.
54 W. Zhang, X. Li, X. Guo and R. Yang, *Polym. Degrad. Stab.*, 2010, **95**, 2541–2546.
55 B. X. Yang, J. H. Shi, K. Pramoda and S. H. Goh, *Compos. Sci. Technol.*, 2008, **68**, 2490–2497.
56 H. Yang, C. Shen, Y. Wang, Y. Su, T. Yang and H. Gao, *Nanotechnology*, 2004, **15**, 70.
57 J. Zhu, K. Kailasam, A. Fischer and A. Thomas, *ACS Catal.*, 2011, **1**, 342–347.
58 C. Beyler and M. Hirschler, *SFPE handbook of fire protection engineering*, 2002, pp. 110–131.
59 B. Singh and N. Sharma, *Polym. Degrad. Stab.*, 2008, **93**, 561–584.
60 S. H. Lee, E. N. R. Cho, S. H. Jeon and J. R. Youn, *Carbon*, 2007, **45**, 2810–2822.
61 J. Kim, S. M. Hong, S. Kwak and Y. Seo, *Phys. Chem. Chem. Phys.*, 2009, **11**, 10851–10859.
62 P. M. Wood-Adams, J. M. Dealy, A. Willem deGroot and O. D. Redwine, *Macromolecules*, 2000, **33**, 7489–7499.
63 S. Li, P. K. Järvelä and P. A. Järvelä, *J. Appl. Polym. Sci.*, 1999, **71**, 1649–1656.
64 M. J. Solomon, A. S. Almusallam, K. F. Seefeldt, A. Somwangthanaroj and P. Varadan, *Macromolecules*, 2001, **34**, 1864–1872.
65 J. K. Mishra, K. J. Hwang and C. S. Ha, *Polymer*, 2005, **46**, 1995–2002.
66 J. Fujiyama-Novak and M. Cakmak, *Macromolecules*, 2008, **41**, 6444–6452.
67 D. H. Kim, P. D. Fasulo, W. R. Rodgers and D. R. Paul, *Polymer*, 2007, **48**, 5308–5323.
68 D. W. Chae, K. J. Kim and B. C. Kim, *Polymer*, 2006, **47**, 3609–3615.
69 P. Pötschke, M. Abdel-Goad, I. Alig, S. Dudkin and D. Lellinger, *Polymer*, 2004, **45**, 8863–8870.